Unusual strain relaxation mechanism in metastable β Ti-Nb alloy after rapid solidification

Wenhao Lin, Helge Heinrich, Ji Ma*[1]

Department of Material Science and Engineering, University of Virginia, Charlottesville, VA 22904, United States of America

Abstract

In this study, an unusual structural distortion in metastable β Ti-Nb was observed after laser melting. Selected area diffraction patterns (SADPs) from transmission electron microscopy (TEM) reveal that after rapid solidification from laser scans in a Ti-25Nb (at.%) sample, a difference in crystal structure was observed between the cellular solidification interior and the intercellular regions. While the intercellular regions remained the bcc (β) phase, the structure of the cell interior dis not match either β or the α'' martensite. Instead, this structure can be interpreted either as an ordered orthorhombic structure with significantly different lattice parameters compared to α'', or a distorted β with 8% strain along with one of the $< 100 >_\beta$ directions with selected variants of nanodomains which originate from the relaxation of interstitial oxygen atoms.

Keywords: Additive manufacturing; Metastable beta titanium; Nanodomains; Rapid solidification

Laser metal additive manufacturing (AM) is an emerging technique for fabricating metal parts. Techniques such as direct energy deposition (DED) and powder bed fusion (PBF) have been widely adopted commercially. Existing alloy systems have been continuously re-introduced to additive manufacturing, and numerous new alloys systems optimized for additive manufacturing are being created. Beyond simplifying the fabrication of customized and/or geometrically complex parts, AM also unlocks unique material physics such as hierarchical solidification microstructures [1]. Laser AM methods create high heating/cooling rates during melting and solidification, which allows the material to develop nano-scale cellular solidification structures [2,3]. The hierarchical microstructures produced by such solidification conditions are believed to significantly improve material performances [2–6]. The difference in composition between cell interior and inter-cellular boundaries can sometimes trigger unexpected precipitation of second phases at the boundaries [5,7–10]. High dislocation densities are also observed in network configurations rooted around the inter-cellular boundaries [11,12]. These dislocation networks are considered to contribute to the high strength and high ductility in additive manufactured 316L stainless steel, breaking the strength-ductility trade-off [12].

---

[1] *Corresponding author.

326 Wilsdorf Hall395 McCormick Road
Charlottesville, Virginia 22904

Email address: jm@virginia.edu

In this study, we investigate the microstructure of laser-processed metastable β titanium-niobium (Ti-25at%Nb) alloy. We utilize the single-track technique to study the effect of rapid solidification conditions on the microstructure of the Ti-Nb alloy. The study was conducted using an Laser powder bed fusion (LPBF) system in order to simulate realistic AM fabrication conditions.

Ti-25Nb (at%) billet produced by vacuum arc melting was solution heated at 900℃ for 2 hrs in an argon atmosphere and water quenched. A 10 mm x 10 mm x2 mm sample was cut from the billet and laser-scanned with an SLM 125 (SLM Solutions, Inc.) laser powder bed fusion system. A laser power of 225 W, scanning speed of 800 mm/s, and hatch distance of 120 μm were used. The schematic of the "single-layer" build can be seen in Fig.1 A). During the laser scanning, the process chamber was held below 1000 ppm oxygen using ultra-high purity argon gas. After laser scans, the substrate was cut perpendicular to the scanning direction, and a cross-section of the scan tracks was extracted for microscopy. $\theta/2\theta$ X-ray powder diffraction (XRPD) was performed using an Empyrean X-ray Diffractometer (Malvern-Panalytical) with a Cu K-α X-ray source. XRD spectra of the sample with the condition before and after the laser scans were captured. Then this thin slice was mechanically polished to 0.05 nm colloidal silica. In order to improve imaging, the sample was etched with 2% (vol.) hydrofluoric acid and 6% nitric acid mix (balanced distilled water). A Quanta 650 (Thermo Fisher Scientific) scanning electron microscope (SEM) was used to observe melt pool geometry and microstructure. A sample for transmission electron microscopy (TEM) was fabricated by focused ion beam (FIB) processing using a Helios UC G4 dual beam system (Thermo Fisher Scientific). TEM imaging was conducted on a Titan 80-300 kV (Thermo Fisher Scientific) transmission electron microscope.

Multiple overlapped melt pools (MPs) can be seen in the optical darkfield image shown in Fig.1 A). Based on the comparison of the XRD spectra in Fig.1 B) acquired before and after the laser scans, the lattices inside the melt pools existed as dominant β (BCC) phase with additional orthorhombic α''martensite phase. To further investigate the microstructure, a TEM sample that spans across the melt pool boundary was prepared by FIB at the location indicated in Fig.1 C). This TEM sample consists of three regions: the heat affected zone (HAZ), the melt pool (MP) boundary, and inside of the MP. These needle-like plates can be recognized as martensite in the HAZ [13]. Even though the induced thermal stress during the laser scanning may partially transform β phase to α'' martensite, no clear sign of martensite was observed within the MP. Instead, significant contrast corresponding to the cellular solidification structures was observed, as shown in Fig.1 C). The cells are separated by the inter-cellular regions which can be identified by their darker contrast. A gradual transition from the HAZ to MP occurs within the 3-4 μm thick MP boundary. Further examination of the structure and the microstructure of the inner MP region is the focus of this study.

Crystal structure analysis of the MP is presented in Fig.2 A). SADPs were taken from the cell, the inter-cellular zone, and the area containing both regions. The bright field (BF) image in the $[200]_\beta$ zone axis is shown in Fig.2 A), with the locations of the selective area aperture indicated as circles with different colors. The corresponding diffraction patterns can be found in Fig.2 B), C), and D) with color-coded circles indicating the central diffraction spot. While the reciprocal lattices of both regions appear identical at first glance, the locations of the diffraction spots are slightly shifted as seen in Fig.2 D). The β lattice parameters within the unmelted regions of the sample correspond well with the values reported by Kim et al. [14]. However, the d-spacing of $(002)_{\beta}$ planes in the cell was found to be 0.178 nm, expanded 8% compared to the theoretical value of 0.1649 nm [14] as well as the β lattice parameters within the unmelted regions of the sample. On the other hand, no such distortion was observed for the $(020)_{\beta}$ planes in the cell. This tetragonal distortion was confirmed from diffraction studies along multiple zone axes,. Interestingly, no such distortion was found in the inter-cellular regions, where the structure could be unambiguously indexed as β (Fig. 2C). Comparing with the real space image of Fig.2 A), the direction of the distortion was perpendicular to the solidification direction of the cells. Moreover, additional diffraction spots appear in the SADPs along the $[31\bar{1}]_{\beta}$ zone axis, shown in Fig.2 G). These spots are located halfway between the $[1\bar{1}2]$ spots in the diffraction pattern, and cannot be produced by the basic β structure. We also note that no diffraction spots corresponding to the ω precipitate was observed anywhere within the melt pool.

Furthermore, the structure in the cell interiors cannot be indexed as α''martensite for two main reasons. First, while it is possible to interpret the structure as orthorhombic, the calculated lattice parameters based on the measured SADPs from a variety of zone axes are 0.355 nm, 0.462 nm, and 0.469 nm. The simulated α''(Cmcm space group) diffraction patterns with such parameters using SingleCrystal 4 software match well with the measured SADPs, shown in Fig.3 A) & B). Yet, according to available studies on the martensite structure, it is impossible to obtain such lattice parameters for α'' phase at any Nb composition[14]. Therefore, the deviation of lattice parameters cannot originate from microsegregation during the rapid solidification. Second, the additional superlattice spots observed in Fig.2 G) are still forbidden spots for the disordered α'' phase in Fig.3 B) based on the simulation. These superlattice spots are also unlikely to be originated from double diffraction phenomenon. No fundamental reflection pairs that can produce such superlattice reflections at the $< 121 >_{cmcm}$ zone axis. The only possible zone axis is $< 112 >_{cmcm}$, considering $\{11\bar{1}\}_{cmcm}$ and $\{1\bar{1}0\}_{cmcm}$ reflections together can introduce $\{20\bar{1}\}_{cmcm}$ as double diffraction reflections. However, this still cannot explain the fact that the intensity of $\{1\bar{1}0\}_{cmcm}$ and $\{20\bar{1}\}_{cmcm}$ spots can be reduced in a similar rate when the sample is tilted away from the zone axis.

A new orthorhombic crystal model is proposed which can produce those superlattice spots, shown in Fig.3 C) & D). The Nb atoms are located at (0, ¾, ¾) and (½ , ¾ , ¼) lattice sites while Ti atoms are found at (½ , ¼ , ¾) and (0, ¼ , ¼) lattice sites. This model requires long-range ordering and therefore no longer possess Cmcm symmetry, and to our knowledge, no report of such structure exists in literature for metastable beta-titanium alloys. Nevertheless, it is one possible interpretation of the structure within the cellular solidification features. Or this unidentified structure can be treated as an intermediate orthorohombic phase like R phase in NiTi[15]. The formation of this distorted orthorohombic phase can help relief stress accured during solidification. No concrete evidence can support this claim yet.

Another possible explanation for this structure is that of a distorted β with selected nanodomain variants. It was reported that the presence of interstitial oxygen in some β-Ti alloys can activate short-range $\{110\}_{\beta} < 1\bar{1}0 >_{\beta}$ transverse shufflings in the form of nanodomains [15–

18] to reduce lattice strain from oxygen atoms situated within the octahedral interstitial sites [18,19]. The oxide layer formed on the sample surface prior to laser melting or oxygen within the environment of the build chamber can be the source of oxygen interstitials. While the diffraction pattern of nanodomains are often show diffuse streaks along with certain crystallography directions[19], they may also manifest as sharp nanodomain diffraction spots after certain thermomechanical processes such as cold rolling, which can act as a mechanism of selection of nanodomain variants to favor certain strain fields [20]. Therefore, We speculate that the extra diffraction spots along $[31\bar{1}]_\beta$ zone axis may originate from such nanodomains. Similar to the variant selection from cold rolling [20] the tetragonal distortion in cells may generate a similar variant selection effect as it creates a larger octahedral interstitial site along the direction of the distortion. As Fig.4 A) indicates, only selected variants such as V2 to appear in cells. Of course, the distortion itself may not necessarily prompt V2 lattice modulation as it can be seen in Fig.4 B), however, the 8% strain along $[001]_\beta$ can be strong enough to prevent other modulations on $\{110\}_\beta$ and $\{101\}_\beta$ planes. Nevertheless, further work is required to determinet the validity of this hypothesis, as well as which of the two interpretation is more plausible for the observed structure within the cellular solidification features.

In summary, we observe significant change in the crystal structure within the cellular solidification features of a Ti-25Nb (at%) alloy after laser processing that simulates the laser AM process. Based on SADPs from the cells, the lattice structure can be interpreted neither β phase or α'' martensite. Two possible explanations are given in the discussion – either a new orthorhombic structure with long-range ordering or highly distorted β with selected variants of nanodomains. More future studies are needed to validate both hypotheses. On the other hand, the intercellular regions were unambigiously indexed as the bcc (β) phase. No ω precipitates were observed anywhere within the melt pool. It is expected that these major changes in structure and microstructure will also create significant changes in the properties of the alloy after laser AM processing.

Acknowledgements

This work is supported by National Science Foundation Grant #2104839 (NSF DMR-MMN). The authors acknowledge Dr. Eric Hoglund for excellent discussions on interpretation of the structures.

Figures

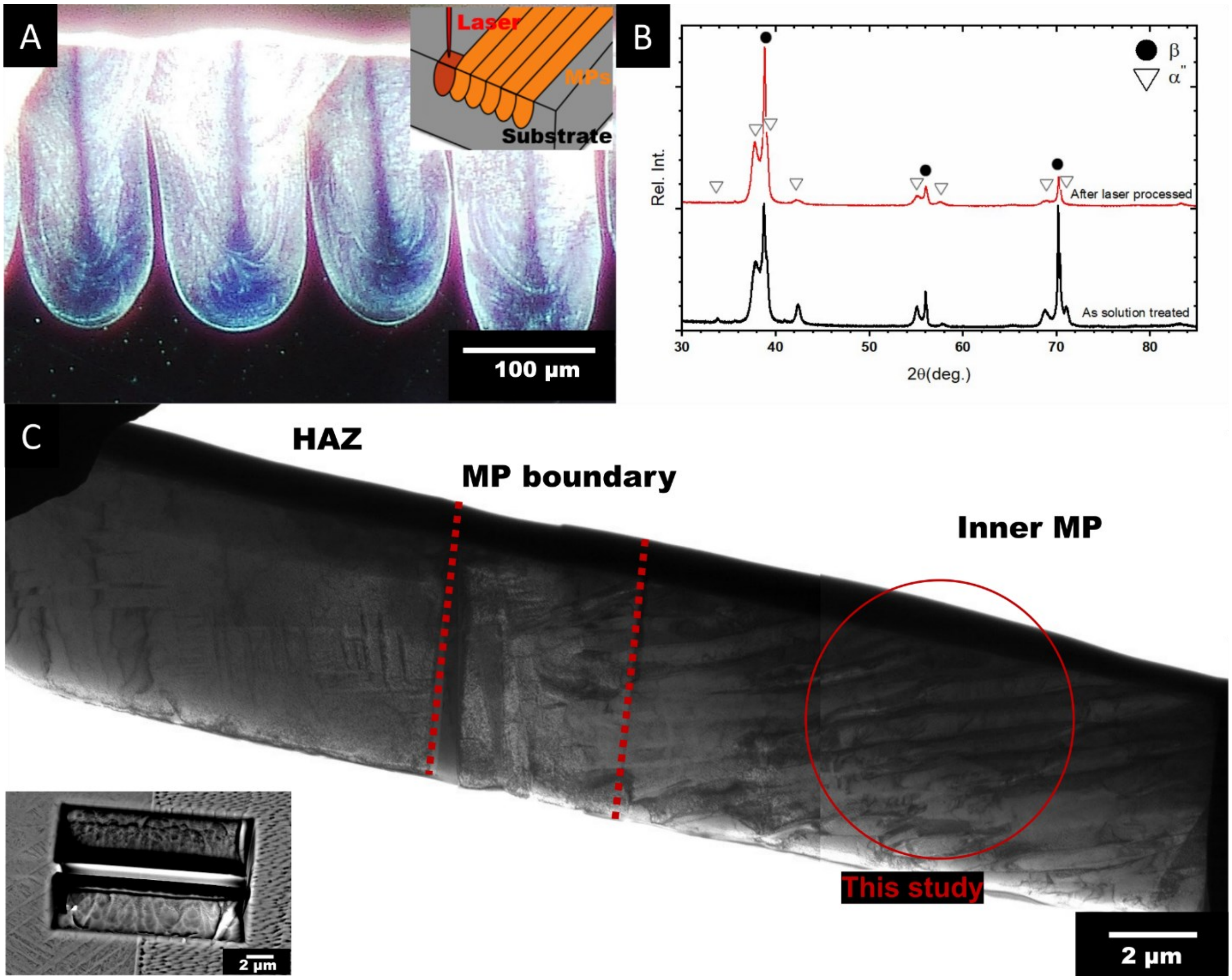
A
Laser
MPs
Substrate
100 µm
B
β
α''
Rel. Int.
After laser processed
As solution treated
30
40
50
60
70
80
2θ(deg.)
C
HAZ
MP boundary
Inner MP
This study
2 µm
2 µm

Figure 1. The microstructures of the melt pool and TEM sample. A) An optical darkfield image of the array of melt pools of Ti-25Nb (at%) with a schematic of a single layer scan on the substrate. B) Comparison between XRD spectrums of the as solution treated condition and post-laser processed condition. C) A BF TEM image, with red dash lines indicating three distinct regions, HAZ, MP boundary, and inner MP. Each region exhibits completely different morphologies. The HAZ mainly consists of the β phase and martensite, whereas the inner MP consists of cellular structures and inter-cellular boundaries. Also, a zoom-in BSE image below indicates where the TEM sample was fabricated.

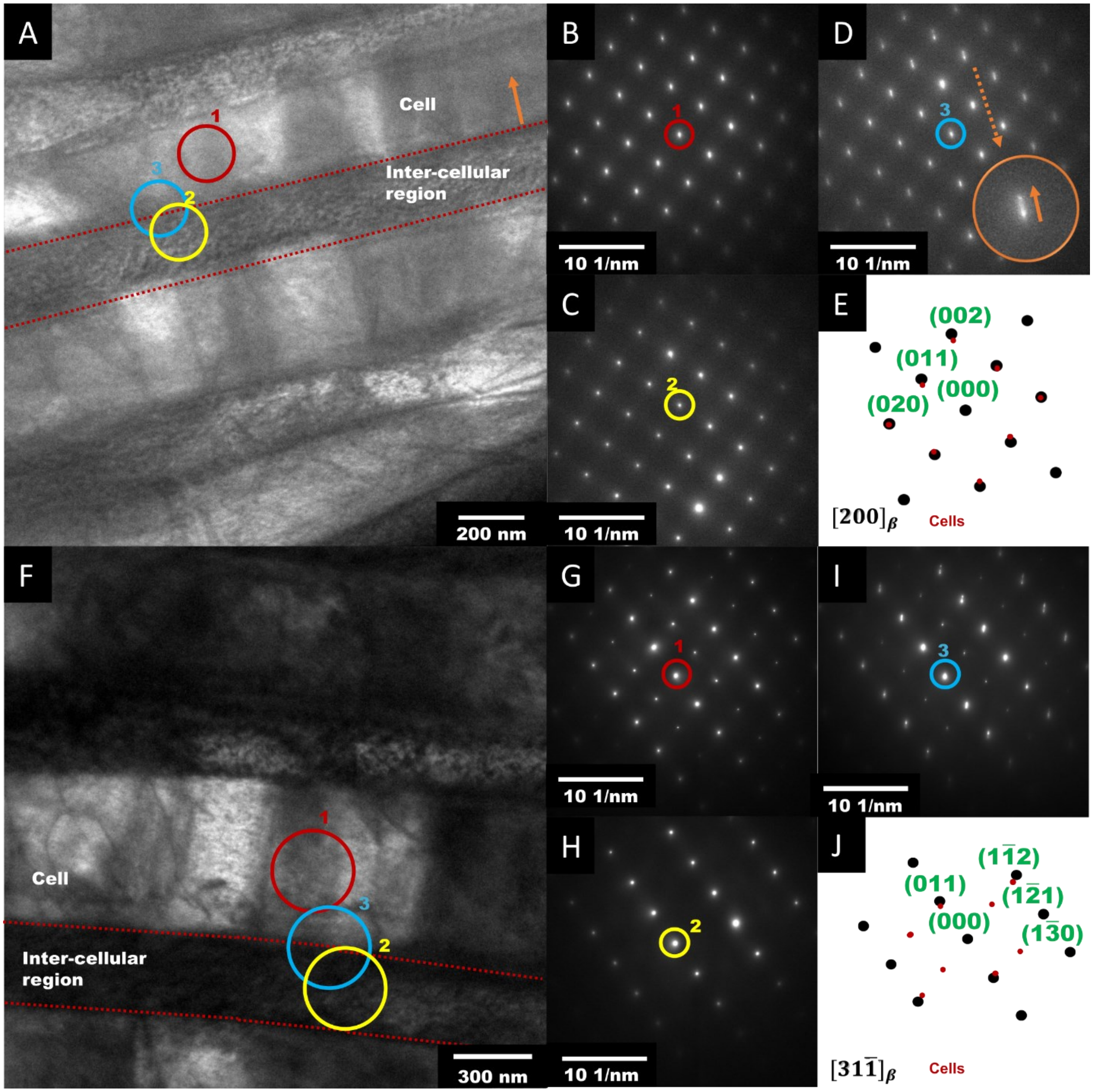

Figure 2. BF images and SADPs of three locations in the $[200]_\beta$ and $[31\bar{1}]_\beta$ zone axes. A) & F) The BF image contains several cells and inter-cellular regions within the inner MP. The locations of selective area aperture marked as circles of red, blue, and yellow, corresponding to the resulted SADP in B) & G), C) & H), and D) & I). For each SADP image, the 000 spots are circled with the same color in A) & F). The schematic diffraction patterns are provided in E) & J). In D), the lattice of the cell is slightly expanded compared to the one of the cellular region. The direction of the expansion is roughly perpendicular to the interface. In G), it shows an additional set of diffraction spots that appear in the cell.

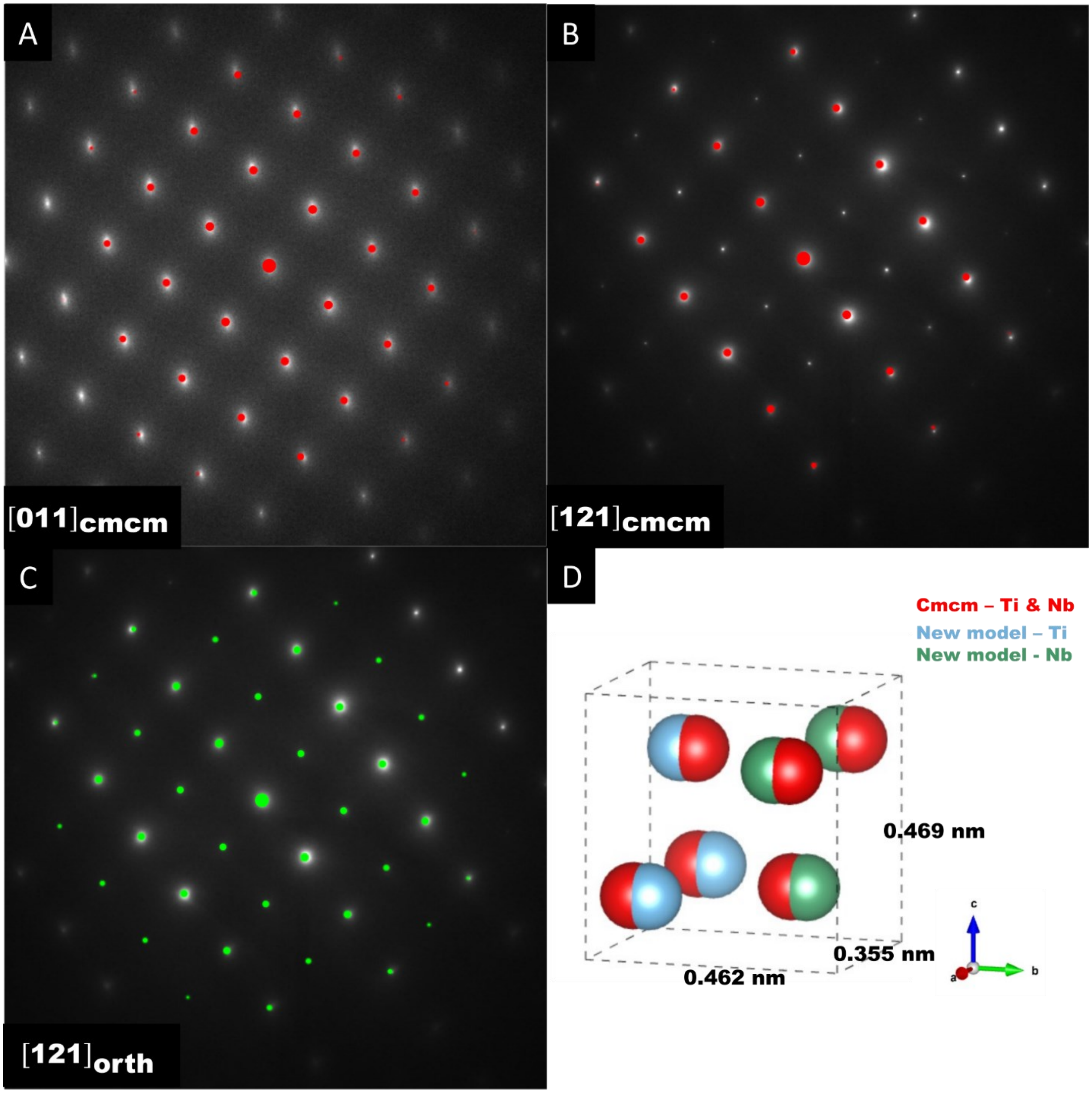

Figure 3. Simulated diffraction patterns overlay on the SADPs from Fig.2 B) & G). The red spots in A) & B) represent the simulated α'' martensite diffraction patterns at $[011]_{cmcm}$ and $[121]_{cmcm}$ zone axes. Similarly, the greed spots in C) represent the simulated diffraction pattern of a proposed orthorhombic model at $[121]_{orth}$ zone axis. D) is the schematic comparison between the Cmcm space group and the proposed model. Note that the diffraction spots are simulated based on the calculated orthorhombic lattice parameters.

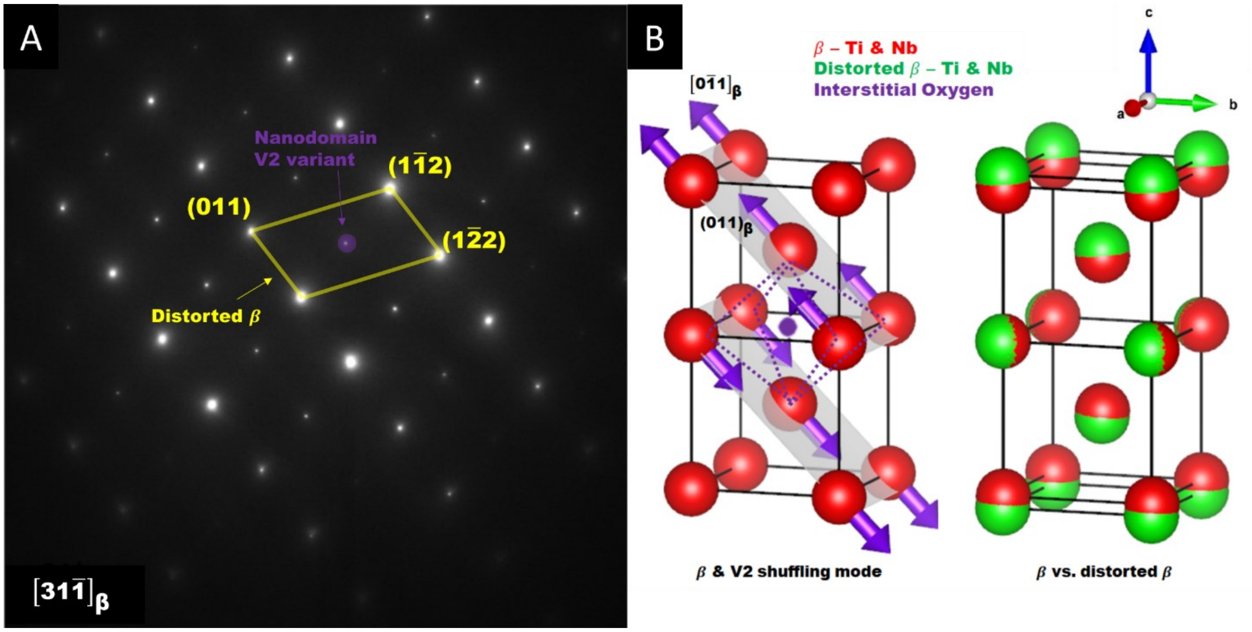

Figure 4. An alternative explanation for the SADP in Fig.2 G). A) the diffraction pattern can be interpreted as the outcome of distorted β phase plus V2 variant nanodomains. B) A schematic explanation of the V2 shuffling mode due to the existence of interstitial oxygen atoms in β structure, which produce V2 variant of nanodomains. A schematic comparison between β and the proposed distorted β phase is shown as well.

References:

[1] N. Li, S. Huang, G. Zhang, R. Qin, W. Liu, H. Xiong, G. Shi, J. Blackburn, J. Mater. Sci. Technol. 35 (2019) 242–269.

[2] T. DebRoy, H.L. Wei, J.S. Zuback, T. Mukherjee, J.W. Elmer, J.O. Milewski, A.M. Beese, A. Wilson-Heid, A. De, W. Zhang, Prog. Mater. Sci. 92 (2018) 112–224.

[3] J.P. Oliveira, T.G. Santos, R.M. Miranda, Prog. Mater. Sci. 107 (2020) 100590.

[4] Z. Zhu, W. Li, Q.B. Nguyen, X. An, W. Lu, Z. Li, F.L. Ng, S.M. Ling Nai, J. Wei, Addit. Manuf. 35 (2020) 101300.

[5] Y. Li, K. Chen, R.L. Narayan, U. Ramamurty, Y. Wang, J. Long, N. Tamura, X. Zhou, Addit. Manuf. 34 (2020) 101220.

[6] P. Deng, H. Yin, M. Song, D. Li, Y. Zheng, B.C. Prorok, X. Lou, JOM 72 (2020) 4232–4243.

[7] A. Hadadzadeh, B.S. Amirkhiz, A. Odeshi, M. Mohammadi, Mater. Des. 159 (2018) 201–211.

[8] Y.S.J. Yoo, T.A. Book, M.D. Sangid, J. Kacher, Mater. Sci. Eng. A 724 (2018) 444–451.

[9] Y. Zhao, Q. Guo, Z. Ma, L. Yu, Mater. Sci. Eng. A 791 (2020) 139735.

[10] Z. Li, Z. Li, Z. Tan, D.B. Xiong, Q. Guo, Int. J. Plast. 127 (2020) 102640.

[11] K.M. Bertsch, G. Meric de Bellefon, B. Kuehl, D.J. Thoma, Acta Mater. 199 (2020) 19–33.

[12] L. Liu, Q. Ding, Y. Zhong, J. Zou, J. Wu, Y.L. Chiu, J. Li, Z. Zhang, Q. Yu, Z. Shen, Mater. Today 21 (2018) 354–361.

[13] Y.W. Chai, H.Y. Kim, H. Hosoda, S. Miyazaki, Acta Mater. 57 (2009) 4054–4064.

[14] H.Y. Kim, Y. Ikehara, J.I. Kim, H. Hosoda, S. Miyazaki, Acta Mater. 54 (2006) 2419–2429.

[15] S. Miyazaki, Shape Mem. Superelasticity 3 (2017) 279–314.

[16] M. Tahara, H.Y. Kim, T. Inamura, H. Hosoda, S. Miyazaki, J. Alloys Compd. 577 (2013) S404–S407.

[17] M. Bönisch, M. Calin, L. Giebeler, A. Helth, A. Gebert, W. Skrotzki, J. Eckert, J. Appl. Crystallogr. 47 (2014) 1374–1379.

[18] Y. Nii, T.H. Arima, H.Y. Kim, S. Miyazaki, Phys. Rev. B - Condens. Matter Mater. Phys. 82 (2010) 214104.

[19] M. Tahara, H.Y. Kim, T. Inamura, H. Hosoda, S. Miyazaki, Acta Mater. 59 (2011) 6208–6218.

[20] H.Y. Kim, L. Wei, S. Kobayashi, M. Tahara, S. Miyazaki, Acta Mater. 61 (2013) 4874–4886.